Measurement of thermo-optic and coating Brownian noise in a novel coating design

Namisha Chabbra, Andrew Wade, and Kirk McKenzie
Center for Gravitational Astrophysics, The Australian National University, 38 Science Rd, Acton ACT 2601 Australia

Nicholas Demos, Slawomir Gras, and Matthew Evans
LIGO, Massachusetts Institution of Technology, NW22-295, 185 Albany St, Cambridge, Massachusetts 02139, USA

(Received 5 June 2025; accepted 8 August 2025; published 6 October 2025; corrected 12 November 2025)

Current gravitational wave detectors and other high precision instrumentation are limited by the optical quality and thermal noise properties of highly reflective dielectric optical coatings. This study characterizes a custom designed high reflectivity optical coating using silica and tantalum pentoxide (SiO_2 and Ta_2O_5) on an ultralow-expansion glass substrate. This coating has been designed to have high thermal noise properties for a future experiment that aims to reduce the effect of Brownian coating noise. This paper presents, to our knowledge, the first measurement of thermo-optic noise for a $SiO_2:Ta_2O_5$ coating. We also present the coating design process of the unique coating and verify modeled coating properties, including transmission, absorption, Brownian coating noise, and thermo-optic noise. With a better understanding of thermo-optic noise and Brownian noise of unique coatings, the design process for optimizing optical coating for lower thermal noise can be better informed, such that the sensitivity of gravitational wave detectors and other precision instrumentation using highly reflective optical coatings is increased.

DOI: 10.1103/n7pr-fr2n

I. INTRODUCTION AND MOTIVATION

Highly reflective optical coatings are an important technology in many high precision laser measurement systems. Highly reflective coatings have applications in ground and space-based gravitational wave detection [1,2], and in high precision optical instrumentation applications such as metrology [3,4], atomic spectroscopy and clocks [5,6], and tests of fundamental physics such as Lorentz invariance [7]. Laser line dielectric coatings are a well established field of research, the driving force of which is to characterize and mitigate the effects of thermal noise that is dominated by Brownian motion, and also contributed to by thermo-optic effects. This thermal noise poses a limit to not only gravitational wave detection but also many of the aforementioned high precision instrumentation applications. For example, Brownian coating thermal noise is currently a limit to the sensitivity of gravitational wave detectors between the frequency of 50 to 200 Hz [1,8]. This directly affects the sensitivity of the detector in this frequency range, limiting the number and fidelity of detected gravitational wave events. Work in this field ranges from experiments that seek to refine the properties of coating materials [9,10], characterizing coatings under cryogenic cooling [11], altering the readout technique in these precision instrumentation applications [12], the coating design and application itself [13], and optimizing mirror manufacturing and shaping [14].

This paper presents, to our knowledge, the first results that experimentally measures thermo-optic noise for a silica and tantalum pentoxide ($SiO_2:Ta_2O_5$) coating. Typically, thermo-optic noise is designed out of optical coatings [15] or is dominated by Brownian thermal noise and is unmeasurable. We have designed a custom coating with similar levels of thermo-optic and Brownian noise, giving us the opportunity to measure both. We outline the design of this novel coating, which will be implemented in an experiment that will demonstrate thermal noise reduction through improved cavity readout, as proposed in [12]. We make use of detailed analytical models of Brownian noise, thermo-optic noise, transmission, and absorption. These models are verified by experimental data. Much work has been done to predict the thermal noise of coatings optimized for lower thermal noise, however by making a measurement of the thermal noise properties of a coating designed for high Brownian noise, the integrity and understanding of the models are also strengthened.

Published by the American Physical Society under the terms of the Creative Commons Attribution 4.0 International license. Further distribution of this work must maintain attribution to the author(s) and the published article's title, journal citation, and DOI.

II. BACKGROUND THEORY ON HIGHLY REFLECTIVE COATINGS

A. The standard quarter-wave stack design

Highly reflective (HR) dielectric and crystalline coatings offer low optical loss from scattering, absorption, and transmission. State-of-the-art coatings are routinely designed to have a loss of 10 ppm (parts per million) or less. HR coatings designed for laser light typically utilize stacked pairs of thin dielectric layers with differing refractive indices to create a highly reflective interface. This coating "stack" is made up of alternating layers of two materials of low and high refractive indices. The layers are typically a quarter-wavelength thick to ensure the constructive interference on reflection at these interfaces. This compounding effect increases the overall reflectivity of the mirror as more layers are added. Figure 1 shows a typical coating design, consisting of doublets of alternating refractive index layers. The quarter-wave stack (QWS) design requires the optical length of each layer to be a quarter of the optical wavelength, such that $n_L d_L = n_H d_H = 0.25 \times \lambda$, where n is the refractive index, d is the physical thickness, and L and H subscripts denote low and high index materials, respectively. In principle, the greater the number of compounding doublets, the higher the proportion of the reflected light. However, due to intramaterial losses, such as absorption, point defects, scattering, and dispersion, there are practical manufacturing limits imposed on the reflectivity of these HR mirrors. Figure 5 shows an ideal reflectivity function in light blue (ii) for a typical 22 QWS coating, centered around 1064 nm, the wavelength used for this study. The transmission for a coating like this is on the order of 1 ppm or less, see Table IV.

B. Thermal noise and absorption in optical coatings

A typical use case for optical mirrors with HR coatings is to create optical resonators or cavities. These resonators act as ultraprecise frequency references to stabilize laser frequency, which is a fundamental prerequisite for interferometric measurements of relative distance and atomic spectroscopy. However, ultimate laser stability is limited by various intrinsic and environmental noises occurring within these optical resonators. This paper will focus on two types of coating thermal noises in optical mirrors, Brownian noise and thermo-optic noise. Optical absorption is also characterized and measured in this work. Photothermal noise was also considered in this work, however is not discussed in this paper as our models predict it is much lower than the Brownian and thermo-optic noise of the designed coating for this work, in the measurement frequency band of interest.

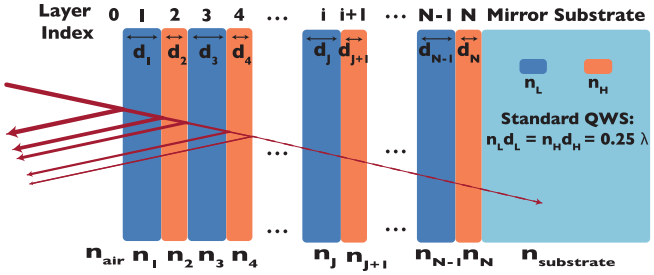


FIG. 1. Standard quarter-wave stack (QWS) coating design. The stack is made up of alternating layers of low and high index materials with quarter-wave optical thicknesses, such that $n_L d_L = n_H d_H = 0.25 \times \lambda$, where n is the refractive index, d is the physical thickness, and L and H subscripts denote low and high index materials, respectively. This allows light to build up constructively as it gets reflected at the interfaces and deconstructively interfere on transmission as it travels into the coating, thus increasing the total reflectivity of the mirror.

1. Brownian thermal noise

Brownian motion is a fundamental physical phenomenon described as intrinsic mechanical motion, due to internal mechanical loss and the temperature of the system. The source of this loss is typically attributed to impurities, stress, and dislocations. This causes random motion within the material in all degrees of freedom, which can imprint onto a laser beam interacting with optical mirrors and coatings. This random length fluctuation couples in noise for gravitational wave detectors, masking true astrophysical signals. According to Hong *et al.* in 2013 [16], Brownian thermal noise of a multilayer coating is contributed to by three factors: thickness fluctuation of the coating layers, fluctuation of the coating-substrate interface, and refractive index fluctuations of the coating layers. These models were further developed by Yam *et al.* in 2015 [17] and Tait *et al.* in 2020 [18], to give Eqs. (1) and (2). These models assume that changes in the ratio of shear to bulk mechanical loss do not significantly change the level of thermal noise and that photoelastic effects are small. The power spectral density of Brownian coating thermal noise in units of displacement is given by in Eq. (1), where b_j is the weighting factor for each layer given in Eq. (2). $S^{\mathrm{Br}}_{\Delta z}(f)$ is the power spectral density of Brownian noise due to the coating, in displacement units, k_B is the Boltzmann constant, T is the mean temperature of the system, f is frequency, σ_s and σ_j are Poisson's ratio of the substrate and ith coating layer, r_G is the beam spot radius, Y_s and Y_i are Young's modulus of the substrate and jth coating layer, d_j is the thickness of the jth layer in the coating stack, ϕ_{M_j} is the mechanical loss angle of the jth layer in the coating stack, assuming that shear and bulk mechanical losses are equal ($\phi_{M_j} = \phi_{\mathrm{bulk}} = \phi_{\mathrm{shear}}$), and $\frac{\partial \phi_c}{\partial \phi_j}$ describes the sensitivity of the total coating phase, $\partial\phi_c$, to fluctuations in the round-trip phase, $\partial\phi_j$, in each layer [16–18]:

$$S^{\mathrm{Br}}_{\Delta z}(f) = \frac{2k_B T(1-\sigma_s-2\sigma_s^2)}{\pi^2 r_G^2 f Y_s} \sum_j b_j d_j \phi_{M_j} \qquad (1)$$

$$b_j = \left[\frac{(1-2\sigma_j)(1+\sigma_j)}{(1-2\sigma_s)(1+\sigma_s)}\right]\frac{1}{1-\sigma_j} \times \left[\left(1-n_j\frac{\partial\phi_c}{\partial\phi_j}\right)^2\frac{Y_s}{Y_j}+\frac{(1-\sigma_s-2\sigma_s^2)^2}{(1+\sigma_j)^2(1-2\sigma_j)}\frac{Y_j}{Y_s}\right]. \quad (2)$$

2. Thermo-optic noise

Thermo-optic or "thermodynamic" noise is unique to optical coatings and was first described and formulated by Evans *et al.* in 2008 as a coherent treatment of both thermorefractive and thermoelastic noise coupling into mirror position measurements [19]. Previous formulations, such as those given by Braginsky *et al.* in 2000 [20] or by Levin in 2008 [21], treated these two noises incoherently. The power spectrum of coating thermal fluctuations sensed by a Gaussian beam $S_{\Delta T}^{\mathrm{TO}}$ described by the fluctuation dissipation theorem as heat dissipation, is expressed in Eq. (3), where $S_{\Delta T}^{\mathrm{TO}}$ is in temperature units, k_B is the Boltzmann constant, T is the mean temperature of the system, r_G is the beam spot radius, κ is thermal conductivity, C is heat capacity per unit volume, and f is frequency [19]. $\mathrm{M}(\frac{f}{f_T})$ is a correction factor for low frequencies, when the thermal diffusion length, $r_T = \sqrt{\frac{\kappa}{2\pi f_T C}}$, is of similar magnitude to the beam spot size, such that f_T is the cutoff frequency for when the thermal diffusion length is equal to the beam size, $r_T = r_G$ [22]. See Ref. [22] for the full derivation:

$$S_{\Delta T}^{\mathrm{TO}} = \frac{2}{\pi^{\frac{3}{2}}}\frac{k_B T^2}{r_G^2\sqrt{\kappa C f}}\mathrm{M}\left(\frac{f}{f_T}\right). \quad (3)$$

Thermo-optic noise manifests as fluctuations in the mirror's effective position, $S_{\Delta z}^{\mathrm{TO}}$, which combines the effects of the thermoelastic and thermorefractive mechanisms. Thermoelastic noise is produced by thermodynamic temperature fluctuations in bulk material that are transformed into surface fluctuations through thermal expansion [23], while thermorefractive noise, driven by the same thermodynamic temperature fluctuations, is due to local refractive index changes which in turn cause fluctuations in the phase of light propagating through the material [20]. $S_{\Delta z}^{\mathrm{TO}}$, described in Eq. (4), is the power spectral density of thermo-optic noise due to a high reflectivity coating of at least six doublets, in displacement units. $\bar{\alpha}_c$ is the effective thermal expansion coefficient of the coating, accounting for the position change of the mirror surface due thermal expansion. $\bar{\beta}$ is the effective thermorefractive coefficient of the coating, accounting for the phase change from each layer in the coating due to refractive index change and thermal expansion. $\bar{\alpha}_s$ is the effective thermal expansion coefficient of the substrate, d_c is the physical coating thickness, C_c and C_s are the heat capacities of the coating and substrate, and λ is the laser wavelength [19]. Effective parameters of the coating are calculated as a weighted average based on the physical thicknesses of the low and high index materials that make up the coating stack:

$$S_{\Delta z}^{\mathrm{TO}} = S_{\Delta T}^{\mathrm{TO}}\Gamma_{tc}(f)\left(\bar{\alpha}_c d - \bar{\beta}\lambda - \bar{\alpha}_s d_c\frac{C_c}{C_s}\right)^2. \quad (4)$$

For finite-thickness coatings where the coating thickness d_c is of similar magnitude to the thermal diffusion length r_T, a correction factor, $\Gamma_{tc}(f)$, is required. This correction factor accounts for reduced coherence between thermoelastic and thermorefractive effects at higher frequencies and is multiplied to $S_{\Delta z}^{\mathrm{TO}}$, still assuming that the beam size r_G is much greater than the thermal diffusion length r_T. For more in-depth calculations on this correction factor, see [19].

Given that thermoelastic noise and thermorefractive noise are driven by the same intrinsic thermal fluctuations, the two noise contributions can be added coherently for mirror coatings, as derived in Evans *et al.* [19]. Depending on the material properties of the coating, these two effects can work in opposite directions as the relative sign between them is negative, as seen in Eq. (4). Therefore, coatings can be designed such that thermo-optic noise is suppressed, from the two effects partially canceling each other out [15]. However, there is a limit to how much thermo-optic noise can be canceled out, due to the cost on other coating properties. For example, for a 57 layer standard quarter-wave stack with a transmission of 0.01 ppm, as shown in Table IV, the terms in the brackets of Eq. (4) amount to 0.06 $\frac{\mathrm{nm}}{\mathrm{K}}$, while for a 57 layer coating optimized for only low thermo-optic noise, the bracketed terms come to 7×10^{-5} $\frac{\mathrm{nm}}{\mathrm{K}}$, but the coating will have an undesirable transmission of 96%. For context, the coating used for this study, also shown in Table IV and in Sec. III, is 57 layers and was optimized for high Brownian noise, while maintaining standard levels of thermo-optic noise and low transmission. This coating has a modeled transmission of 5.2 ppm, and the bracketed terms amount to 0.16 $\frac{\mathrm{nm}}{\mathrm{K}}$.

3. Absorption

Coating absorption for a high reflectivity multilayer coating is typically expressed as a coefficient in parts per million (ppm) of the incident optical power on the mirror, and contributes to intracavity losses, reducing the overall cavity optical finesse. Equation (5) shows the calculation of total coating absorption, a_c, which is a sum of the absorption from each layer based on the optical field in each layer, as formulated by Yam *et al.* in 2015 [17]. λ is the optical wavelength, p_j is the optical absorption in the jth layer in the coating stack (for which a full derivation can be found in Ref. [17]), k_j is the extinction coefficient of the jth coating layer, and d_j is the thickness of the jth coating layer. E_0 is the optical field entering the coating from vacuum, E_j is the optical field in the jth coating layer, r_j is

the complex reflectivity of the jth coating layer, n_j is the refractive index of the jth coating layer, and $\bar{r}_j$ is the recursively combined complex coating reflectivity of the jth coating layer and all other layers between it and the substrate:

$$a_c = \frac{4\pi}{|E_0|^2\lambda}\sum_{j=1}^{N}|E_j|^2\rho_j k_j d_j, \quad \text{where}$$

$$\mathrm{E}_{j+1} = \frac{\sqrt{1-r_j^2}}{1+r_j\bar{r}_{j+1}}\mathrm{E}_j, \qquad r_j = \frac{n_j - n_{j+1}}{n_j + n_{j+1}}. \tag{5}$$

As seen in Eq. (5), absorption is affected by the phase of the electromagnetic field at the coating-air interface, E_0, and in each layer, E_j, which are determined by the complex reflectivity calculations for each layer, r_j and $\bar{r}_j$. For a standard QWS design, the phase is 180° or π at the coating surface, as the light deconstructively interferes as it propagates into the coating. The tradeoff of having a non-π phase at the coating-air interface is that additional light propagates into the coating and increases the potential absorption, if the higher loss material constitutes a greater proportion of the coating compared to the lesser loss material. Absorption is an important metric to minimize, to reduce photothermal noises, such as photothermoelastic and photothermorefractive noise, as absorption will couple laser intensity noise into the coating phase response.

III. COATING DESIGN PROCESS

The aim of this design process was to optimize a highly reflective, low transmission coating with high Brownian noise. This was intentional, as a high baseline level of Brownian thermal noise will enable a first experiment demonstrating a novel readout technique to reduce the effect of Brownian noise to begin with. The concept for this experiment and technique based approach is detailed in [12]. Absorption, thermo-optic noise, and phase at the coating-air interface are also considered in this process. As mentioned above, the standard coating for high reflectors is the quarter-wave stack of alternating low and high refractive index materials. Common coating candidates for gravitational wave detectors are silica and tantalum pentoxide (SiO_2:Ta_2O_5) or aluminium gallium arsenide and gallium arsenide (AlGaAs:GaAs).

AlGaAs:GaAs coatings offer low Brownian thermal noise, but at a trade-off of high thermo-optic noise. SiO_2:Ta_2O_5 coatings offer low thermo-optic noise and low absorption, but higher Brownian thermal noise. Therefore, this study uses SiO_2 and Ta_2O_5, due to these favorable optical and mechanical properties [24]. Optimization of the coating was achieved using previous verified code [25], modified to meet the unique requirements of this study. A schematic of the optimization workflow is shown in Fig. 2, adapted from the work of

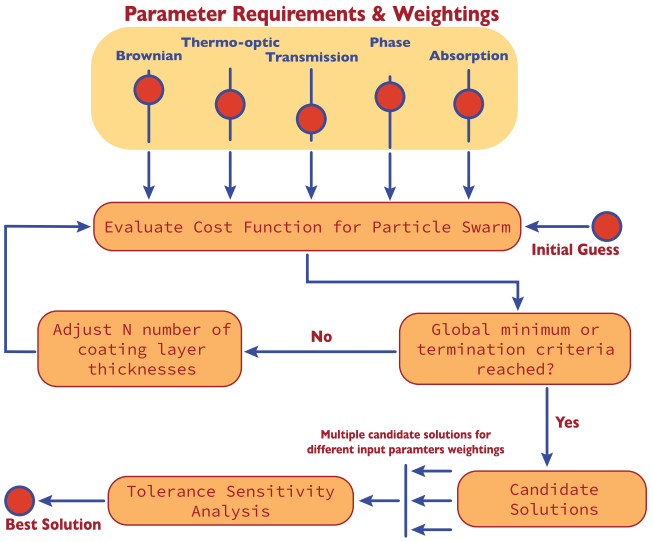


FIG. 2. Schematic of workflow for the coating design and optimization, adapted from the work of Venugopalan *et al.* [26]. A cost function is calculated as the sum of the differences between the calculated and ideal values of five coating properties: Brownian thermal noise, thermo-optic noise, transmission, phase of the electromagnetic field at the coating-air interface and absorption. This cost function is iteratively reduced using a global optimization algorithm that modifies the layer thicknesses of the coating stack until an optimum solution is found. A tolerance analysis is done to ensure the design is robust against random or systematic error in coating application.

Venugopalan *et al.* [26], in which a candidate solution is discovered using the particle swarm method. The optimization process first requires a set of parameters to optimize for, which in this case are

(i) Brownian thermal noise, calculated using Eq. (1), with the material properties in Table I.
(ii) Thermo-optic noise, calculated using Eq. (4) and the thick-coating correction factor, with the material properties in Table I.
(iii) Transmission, calculated using the complex reflectivity equations in Eq. (5) for multilayer coatings derived in [16], using the refractive indices in Table I.
(iv) Phase of the electric field at the output of the coating (coating-air interface), calculated using the complex reflectivity calculated above.
(v) Absorption, calculated using refractive indices and extinction coefficients in Table I and Eq. (5).

Each parameter is calculated for a baseline coating design and a "cost" function is calculated as the sum of the differences between the ideal values of these parameters and the calculated values, where weights can also be applied to each of the parameters in order to prioritize certain coating properties. This cost value is the input to an in-built MATLAB optimization function called particle swarm optimization (PSO), which utilizes efficient methods for global optimization. The PSO function will

TABLE I. Material properties of silica and tantalum pentoxide used for modeling the Brownian thermal noise, thermo-optic noise, transmission, phase, and absorption of various coating structures as part of the design and optimization process.

Parameter	Tantala (Ti_2O_5)	Silica (SiO_2)
Refractive index, n	2.076 [27]	1.466 [27]
Young's modulus, Y (Pa)	1.40×10^{11} [28]	7.27×10^{10} [28]
Poisson's ratio, σ	0.23 [28]	0.167 [28]
Heat capacity, C ($\frac{J}{m^3 K}$)	2.1×10^6 [28]	1.64×10^6 [28]
Thermal expansion coefficient, a (K^{-1})	3.6×10^{-6} [28]	5.1×10^{-7} [28]
Thermorefractive coefficient, β (K^{-1})	1.4×10^{-5} [28]	8.0×10^{-6} [28]
Thermal conductivity, κ ($\frac{W}{mK}$)	33 [28]	1.38 [28]
Mechanical loss Angle, ϕ	$2.29 \times 10^{-4} \times f^{0.079}$ [29]	$1.26 \times 10^{-4} \times f^{-0.069}$ [29]
Extinction coefficient, k	2×10^{-7} [27]	1×10^{-7} [27]

iteratively work to reduce the input cost value by modifying the thicknesses of each of the layers in the coating, within realistic bounds. Once the optimization identifies potential designs, tolerance sensitivity analysis is done, via simulations, to assess robustness. These simulations introduce small, random perturbations as well as systematic errors to layer thicknesses simulating possible manufacturing variances. The best coating design solution is then selected based on the performance from the tolerance sensitivity analysis.

TABLE II. Optimized coating design used for this study. Each layer's material, refractive index, and thickness are specified. This is also visually represented in Fig. 3. Optical thickness is described as a fraction of $\lambda = 1064$ nm. The total optical coating thickness is $d_{opt} = 14.7\lambda$ and the total physical thickness is $d_c = 8.7$ μm. $n_{air} = 1.00$, $n_{Ta_2O_5} = 2.076$, $n_{SiO_2} = 1.466$, and $n_{substrate} = 1.48$.

Number	Layer	Optical thickness	Physical thickness (nm)	Number	Layer	Optical thickness	Physical thickness (nm)
0	Air	…	…	1	Ta_2O_5	0.3259	167.11
2	SiO_2	0.2070	150.33	3	Ta_2O_5	0.3161	162.06
4	SiO_2	0.2082	151.17	5	Ta_2O_5	0.4717	241.86
6	SiO_2	0.3392	246.32	7	Ta_2O_5	0.1714	87.91
8	SiO_2	0.3235	234.91	9	Ta_2O_5	0.1696	86.98
10	SiO_2	0.3222	233.92	11	Ta_2O_5	0.1742	89.35
12	SiO_2	0.3181	230.97	13	Ta_2O_5	0.1824	93.55
14	SiO_2	0.3088	224.25	15	Ta_2O_5	0.1960	100.49
16	SiO_2	0.2922	212.167	17	Ta_2O_5	0.2184	111.96
18	SiO_2	0.2646	192.15	19	Ta_2O_5	0.2538	130.16
20	SiO_2	0.2247	163.15	21	Ta_2O_5	0.2983	152.95
22	SiO_2	0.1869	135.71	23	Ta_2O_5	0.3296	168.99
24	SiO_2	0.1652	119.92	25	Ta_2O_5	0.3451	176.98
26	SiO_2	0.1549	112.48	27	Ta_2O_5	0.3527	180.84
28	SiO_2	0.1495	108.52	29	Ta_2O_5	0.3568	182.95
30	SiO_2	0.1466	106.44	31	Ta_2O_5	0.3595	184.31
32	SiO_2	0.1447	105.05	33	Ta_2O_5	0.3609	185.06
34	SiO_2	0.1437	104.30	35	Ta_2O_5	0.3616	185.42
36	SiO_2	0.1433	104.08	37	Ta_2O_5	0.3620	185.62
38	SiO_2	0.1428	103.68	39	Ta_2O_5	0.3624	185.82
40	SiO_2	0.1425	103.50	41	Ta_2O_5	0.3627	185.97
42	SiO_2	0.1423	103.33	43	Ta_2O_5	0.3629	186.09
44	SiO_2	0.1421	103.21	45	Ta_2O_5	0.3629	186.07
46	SiO_2	0.1422	103.27	47	Ta_2O_5	0.3630	186.13
48	SiO_2	0.1421	103.16	49	Ta_2O_5	0.3631	186.17
50	SiO_2	0.1420	103.12	51	Ta_2O_5	0.3630	186.12
52	SiO_2	0.1422	103.22	53	Ta_2O_5	0.3629	186.09
54	SiO_2	0.1422	103.24	55	Ta_2O_5	0.3630	186.11
56	SiO_2	0.1421	103.16	57	Ta_2O_5	0.3683	188.83
58	Ultralow expansion	…	…				

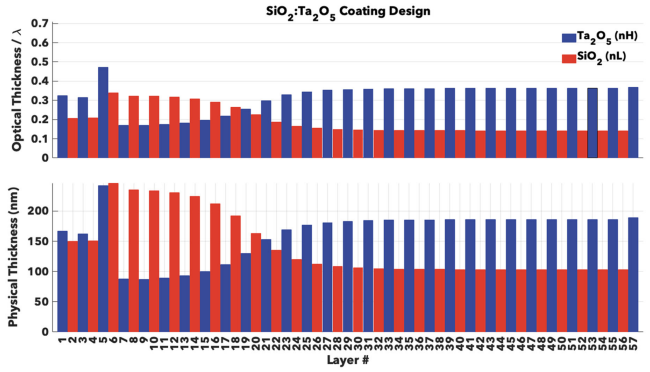


FIG. 3. The optical and physical thicknesses of each layer in the optimized coating design used in this study. This coating design, which has also been tabulated in Table II, does not use a standard quarter-wave stack design, which would be uniformly 0.25λ in optical thickness. Optical thickness is described as a fraction of $\lambda = 1064$ nm. The total optical coating thickness is $d_{opt} = 14.7\lambda$ and the total physical thickness is $d_c = 8.7$ μm. $n_{air} = 1.00$, $n_{Ta_2O_5} = 2.076$, $n_{SiO_2} = 1.466$, and $n_{substrate} = 1.48$.

The final coating design from this process is tabulated in Table II, and is shown in Fig. 3. The material and thermal noise properties of this 57 layer coating design is shown in Table IV, referred to as "Optimized (N = 57)" and accounts for the folded cavity and higher order mode measurement configuration used in this study, which is discussed further in Secs. V and VI. A standard quarter-wave coating with 44 layers is tabulated for reference, as this is a standard coating design for high finesse mirrors, as well as a standard quarter-wave coating with 57 layers to compare with the optimized structure. Our coating design has suitable modeled transmission of 5.2 ppm, as well as suitable thermo-optic noise of $0.86\frac{m}{\sqrt{Hz}} \times 10^{-17}$ at 1 kHz, and high Brownian noise of $1.59\frac{m}{\sqrt{Hz}} \times 10^{-17}$ at 1 kHz, as desired. The total optical coating thickness is $d_{opt} = 14.7\lambda$ and the total physical thickness is $d_c = 8.7$ μm. The phase of the electromagnetic field at the surface of the coating is 80°. The deviation from 180° is due to the trade-off in the optimization process to prioritize high thermal noise properties and low transmission. This is reflected in the abnormally high modeled absorption of 13.12 ppm, which also accounts for uncertainties in the extinction coefficient values of silica and tantalum pentoxide (also referred to as tantala) at 1064 nm [27], which have not been explored in current literature. The extinction coefficient values used from Table I are conservative estimates and therefore there is potential for the measured absorption of the coating to be lower than predicted.

IV. REFLECTION AND TRANSMISSION MEASUREMENTS FROM SUPPLIER

The designed coating was deposited by Five-Nine Optics onto ultralow-expansion glass substrates supplied by Stable Laser Systems, using ion beam sputtering. The deposition parameters were typical production parameters for a commercial Veeco Spector chamber, and the coating was annealed at 480 °C with a 2 hour ramp, 1.5 hour dwell, and 2 hour cool. As such, the mechanical loss angle and frequency dependence in Table I for silica and tantala are based on previous measurements from a Veeco Spector Chamber, annealed at 500 °C [29]. Various coating deposition methods can affect mechanical loss angles of coating materials and is still an active area of research. The values we have used under the given deposition parameters are the most recently reported values for these materials [29], but still may not reflect the exact properties of our coating due to the different annealing temperatures, or a number of other factors, such as differing annealing times, refractive indices and measurement conditions.

Figure 5 shows the modeled transmission for a standard 44 layer quarter-wave stack in light blue (ii), the modeled transmission for our custom coating design from Sec. III in dark blue (iii), and the measured transmission from the coating supplier in orange (i), all centered around 1064 nm, the design wavelength, in gray (iv). The standard 44 layer quarter-wave stack has a minimum transmission of less than 1 ppm around the design wavelength and the "bucket" is wide and uniform in shape. The optimized 57 layer stack model shows a small hump around 1080 nm, due to the unique and nonstandard structure of the coating. However, the transmission around 1064 nm is modeled to be 5.2 ppm and this is verified by a measurement of 3.2 ppm transmission at 1064 nm, as shown in Table IV. The general shape of the modeled and measured transmission of the optimized 57 layer coating show good consistency, with measurement limitations and coating manufacturing tolerances possibly explaining the deviations from the model around 1064 nm, and deviations outside the bucket shape. For example, random thickness error between ±1 nm applied to every layer can change the expected transmission by up to 0.3 ppm at 1064 nm.

V. EXPERIMENTAL SETUP

Two mirror samples with the same coating from Table II and Fig. 3 were measured in this study, which will be referred to as sample 1 and sample 2. The cavity setup for which these mirror samples were characterized can be seen in Fig. 4, which has been taken from Gras *et al.* 2017 in Ref. [9]. The measured cavity parameters during data collection are shown in Table III for sample 1. A folded cavity was used to measure the coating properties and thermal noise on the sample mirror. This is done by taking a differential measurement of two second order Hermite-Gaussian modes, TEM02 and TEM20, as seen in the figure inset. The beatnote of these two modes that are locked and resonating within the cavity is tracked using a phase locked loop, which isolates the changes in the beatnote due to coating thermal noise.

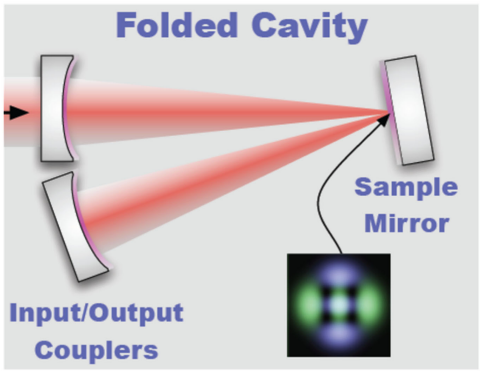


FIG. 4. This figure was taken from Ref. [9]. A folded cavity was used to measure the coating properties and thermal noise of the sample mirror. This is done by taking a differential measurement of two second order Hermite-Gaussian modes, TEM20 and TEM02, as seen in the inset. The beatnote of these two modes that are locked and resonating within the cavity is tracked using a phase locked loop, which isolates the changes in the beatnote due to coating thermal noise.

VI. CORRECTION FACTORS

Coating thermal noise is typically expressed for a single mirror with a Gaussian pressure profile, with assumptions made about the size of the beam and the thickness of the coating. However, as discussed in Sec. V, this experiment uses a folded cavity, higher order modes, and the coating thickness is of similar magnitude to the beam size. Both Brownian noise and thermo-optic noise require a series of corrections to account for these differences, outlined below for power spectral density units:

TABLE III. Measured cavity parameters during collection of the data for sample 1.

Parameter	Units	TEM02	TEM20
Beam size	μm	40	40
Radius of curvature (effective)	mm	50.015	50.057
Mode frequency	MHz	178.228	186.794
Polarization (P-S) splitting	MHz	61.892	
Laser wavelength	nm	1064	
Free spectral range	GHz	1.511	
Cavity length	mm	$L_1 + L_2 = 99.171$	
Folding angle	deg	17.23	
Finesse		58k	

(i) *Correction for "double bounce,"* C_{fold}. The folded cavity configuration involves the laser beam bouncing off the sample mirror twice on the same spot, thus doubling the energy in amplitude spectral density units, or multiplying by 4 in power spectral density units. Therefore the correction for both Brownian and thermo-optic noise is $C_{fold} = 4$.

(ii) *Correction for fringes*, C_{fringe}. Another feature of the folded cavity is that the two propagating beams interfere on the sample mirror and create a fringe pattern [30]. A finite element analysis for Brownian coating noise was done for this in Ref. [9] for a thick coating such as the one used in our study, and was calculated to be 0.98 to correct from a folding cavity to a single beam on a mirror. We assume that this correction is the same for thermo-optic noise, therefore the correction here for both noises is $C_{fringe} = 1/0.98 = 1.03$.

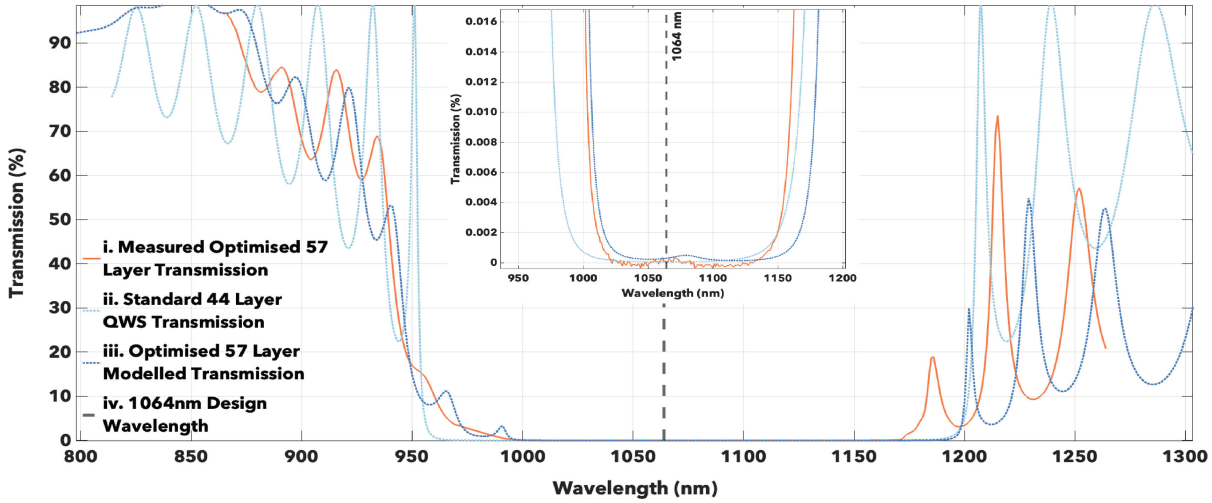


FIG. 5. Measured transmission vs wavelength of the designed coating in orange (i), modeled transmission vs wavelength of a standard 44 layer quarter-wave stack coating in light blue (ii), and the designed 57 layer coating model in dark blue (iii), all centered around 1064 nm in gray (iv). The inset shows that all three curves have low transmission around 1064 nm, below 5 ppm. The general shape of the model and measured transmission of the optimized 57 layer coating show good consistency, with measurement limitations and coating manufacturing tolerances possibly explaining the deviations from the model around 0 ppm transmission, and deviations outside the bucket shape.

(iii) *Correction for higher order modes for Brownian noise*, $C_{HOM\,BR}$. The coating thermal noise measured in this experimental configuration is of the non-overlapping area of the TEM20 and TEM02 modes. A finite element analysis was done in Ref. [9] for a thick coating such as the one used in this study, to correct from the two higher order modes to a Gaussian beam for Brownian noise, and was calculated to be 1.13. Therefore the correction for Brownian noise here is $C_{HOM\,BR} = 1/1.13 = 0.89$.

(iv) *Correction for higher order modes for thermo-optic noise*, $C_{HOM\,TO}$. We cannot assume that the Brownian noise higher order mode correction is the same for thermo-optic noise as the two thermal noises could be affected differently by the intensity profile of the beam. Current models of thermo-optic noise for the fundamental Gaussian TEM00 mode rely on the fact that the beam intensity, and thus the applied pressure on the mirror, reduces uniformly in the x and y directions. Higher order modes, however, do not reduce uniformly in the x and y directions and have "hot spots" which sense the thermal fluctuations from the mirror at different points and different weightings, making it harder to model. A finite element analysis is required to understand the correction factor required for thermo-optic noise, which has not been done before [9,25]. For this study, we sweep possible values of this correction factor and the thick coating correction factor, $C_{d\,BR}$, as seen in Fig. 7 and discussed in Sec. VII B, and use the value for which the model best fits the measured data, which is $C_{HOM\,TO} \times C_{d\,TO} = 0.25$.

(v) *Correction for thick coating for Brownian noise*, $C_{d\,BR}$. A correction is required for the thick coating used in this study. Standard models for Brownian and thermo-optic noise are formulated under a thin coating assumption, where the coating thickness is much smaller than the beam size, $d_c \ll r_G$. Brownian motion is contributed to by all of the layers in the coating stack under the thin coating thickness assumption. However, as $\frac{d_c}{r_G}$ approaches 1, these assumptions break down and thermal fluctuations become less correlated in the spatial domain [9,22]. A finite element analysis is required to calculate this correction factor. For this study, we sweep possible values of this correction factor, as seen in Fig. 7 and discussed in Sec. VII B, and use the value for which the model best fits the measured data, which is $C_{d\,BR} = 0.97$.

(vi) *Correction for thick coating for thermo-optic noise*, $C_{d\,TO}$. We cannot assume that the thick coating correction factor is the same for thermo-optic noise as it is for Brownian noise. Thermo-optic noise is contributed to by the thermoelastic effect in all of the layers of the coating under the finite coating thickness assumption; however, the contribution from the thermorefractive effect is only from the layers within the penetration depth of the coating, and as such a thick coating correction factor may not be needed for the thermorefractive component. A finite element analysis is required to calculate this correction factor. For this study, we sweep possible values of this correction factor and higher order mode correction factor, $C_{d\,BR}$, as seen in Fig. 7 and discussed in Sec. VII B, and use the value for which the model best fits the measured data, which is $C_{HOM\,TO} \times C_{d\,TO} = 0.25$.

Equation (6) shows the final coating thermal noise (CTN) calculation in amplitude spectral density units in the measurement frequency band of 300 to 2.4 kHz, including the correction factors mentioned above, and the expected CTN level at 1 kHz based on our models. This model is also presented in Table IV.

$$\begin{aligned}
\mathrm{CTN}(f) &= \sqrt{C_{BR} \times S^{Br}_{\Delta z}(f) + C_{TO} \times S^{TO}_{\Delta z}(f)}, \\
C_{BR} &= C_{fold} \times C_{fringe} \times C_{HOM\,BR} \times C_{d\,BR} \\
&= 4 \times 1.03 \times 0.89 \times 0.97 = 3.56, \\
C_{TO} &= C_{fold} \times C_{fringe} \times C_{HOM\,TO} \times C_{d\,TO} \\
&= 4 \times 1.03 \times 0.25 = 1.03, \\
\mathrm{CTN}_{model}(f) &= 1.81 \times 10^{-17} \times \left(\frac{1\ \mathrm{kHz}}{f}\right)^{0.450} \frac{\mathrm{m}}{\sqrt{\mathrm{Hz}}}. \qquad (6)
\end{aligned}$$

VII. RESULTS AND DISCUSSION

A. Coating thermal noise and absorption measurements

Table IV shows the modeled coating properties and the corresponding measured values. The beam spot size on sample 1 was 40 μm, as shown in Table III. The cutoff frequency for which the beam size is equal to the thermal diffusion length is $f_T = 160$ Hz. The absorption is lower than expected, which was modeled to be 13.1 ppm and was measured to be 2.7 ppm. To accurately estimate this quantity, both the coating structure and the extinction coefficients must be well known. In our case, the layer structure is precisely defined; however, the extinction coefficients for silica and tantala are only approximate values obtained from the literature, see Table I. Note, extinction coefficients can vary significantly depending on the coating deposition parameters. This variation can be as high as an order of magnitude and often decreases after thermal treatment of the coating. A direct measurement of these coefficients is beyond the scope of this paper. We have assumed a conservative ratio of 2:1 in the extinction coefficients of tantala and silica. The implication of measuring a lower absorption than predicted is either that the ratio between the extinction coefficients of tantala and

TABLE IV. Comparison of four coating designs, assuming a beam spot size of 40 μm, as measured on sample 1, with the correction factors discussed in Sec. VI applied for a folded cavity configuration using higher order modes for measurement and a thick coating. A standard QWS of 44 layers is shown for reference, which is a typical coating design. The properties of a 57 layer QWS coating, before optimization, and the 57 layer optimized coating as modeled and measured are also presented.

Coating design at 1 kHz	Transmission (ppm)	Thermo-optic noise $\left(\frac{\mathrm{m}}{\sqrt{\mathrm{Hz}}} \times 10^{-17}\right)$	Brownian noise $\left(\frac{\mathrm{m}}{\sqrt{\mathrm{Hz}}} \times 10^{-17}\right)$	Total noise $\left(\frac{\mathrm{m}}{\sqrt{\mathrm{Hz}}} \times 10^{-17}\right)$	Phase (deg)	Absorption (ppm)
Standard QWS (N = 44)	0.61	0.27	0.97	1.01	180	0.87
Standard QWS (N = 57)	0.01	0.31	1.01	1.15	180	0.87
Optimized (N = 57)	5.2	0.86	1.59	1.81	80	13.12
Measured (N = 57)	3.2	⋯	⋯	1.81	⋯	2.7

silica in this coating design is lower than 2:1 or that the estimated extinction coefficients are too high, or both.

Figure 6 shows an amplitude spectral density between 325 and 2400 Hz of the measured coating thermal noise of sample 1 in red (i). It should be noted that this measurement band is higher than the cutoff frequency of the coating at this particular beam size, $f_T = 160$ Hz. The orange (ii) and yellow (iii) traces are the residuals of the data when each thermal noise model, Brownian and thermo-optic, are subtracted. The modeled Brownian thermal noise is plotted in dashed dark blue (v) and thermo-optic noise is plotted in dashed light blue (vi). The total noise model in the solid blue line (iv) is the sum of the Brownian noise and thermo-optic noise models, which have been multiplied by the relevant correction factors discussed in Sec. VI, and agrees with the measured data. These models and the measured coating noise in Fig. 6 match the values in Table IV at 1 kHz. The peak at 600 Hz is due to acoustic noise in the environment coupling into the measurement, and does not reflect thermal activity in the sample.

The modeled total noise at 1 kHz is $1.81 \times 10^{-17} \frac{\mathrm{m}}{\sqrt{\mathrm{Hz}}}$, as calculated in Eq. (6). The data for sample 1 was converted into linear form using the base 10 logarithmic function, and then analyzed using a linear fit. This can be seen in Eq. (7), with a 95% confidence interval serving as the error bounds. The measured total noise at 1 kHz is $1.81 \times 10^{-17} \frac{\mathrm{m}}{\sqrt{\mathrm{Hz}}}$, which

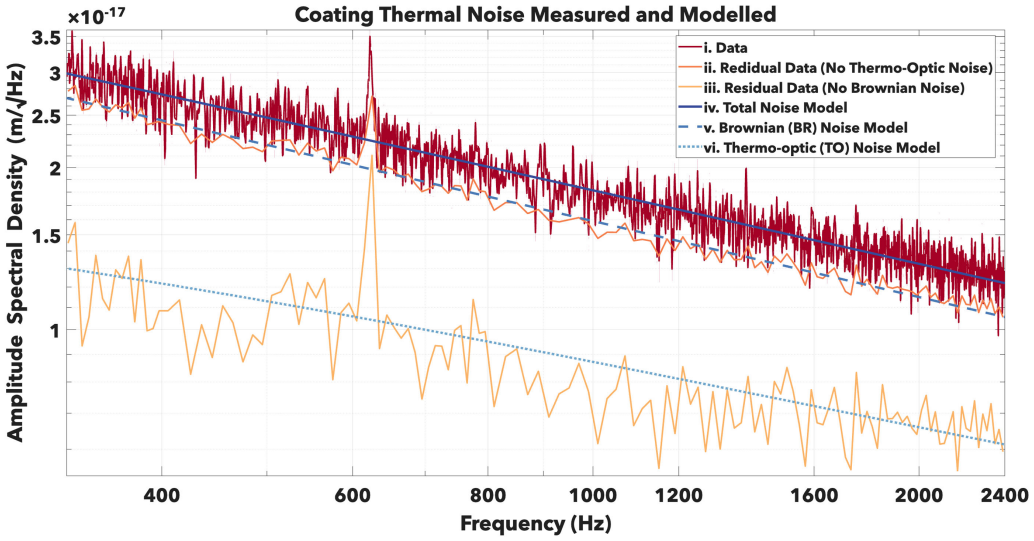


FIG. 6. The amplitude spectral density of sample 1 data is shown. The red trace (i) is the measured spectrum and can be compared to the solid blue line (iv) as the reference model. The orange (ii) and yellow traces (iii) are the residuals of the data when each thermal noise model in the blue dashed lines, Brownian (v) and thermo-optic (vi), are subtracted and compared to the opposite thermal noise model. The two types of noise show good agreement with the relevant residual data. Thermo-optic noise has a slope of $f^{-0.38}$ in this frequency region and Brownian noise has a slope of $f^{-0.47}$. The slope of the total modeled noise is $f^{-0.450}$, which agrees with the measured total noise slope of $f^{-0.443\pm0.007}$ within the 95% confidence interval, indicating that the measured data must have both Brownian noise and thermo-optic noise contributions. The full equations for the modeled total noise and measured total noise can be seen in Eqs. (6) and (7), respectively.

agrees with the model within the 95% confidence interval:

$$\mathrm{CTN}_{\mathrm{S1}}(f) = (1.81 \pm 0.08) \times 10^{-17} \times \left(\frac{1\ \mathrm{kHz}}{f}\right)^{0.443\pm0.007} \times \frac{\mathrm{m}}{\sqrt{\mathrm{Hz}}}. \quad (7)$$

B. Goodness of fit

In order to ensure that the measurement indeed captures both Brownian noise and thermo-optic noise, residuals of the data are plotted in Fig. 6 in orange (ii) and yellow (iii). The data minus the thermo-optic noise model is plotted and shows good agreement with the model for Brownian noise, and the reverse case of the data minus the Brownian noise model shows good agreement with the thermo-optic model. The thermo-optic noise model has a slope of $f^{-0.38}$ in this frequency region and the Brownian noise model has a slope of $f^{-0.47}$. Using a linear fitting function with a 95% confidence interval, the slope of the measured total noise is $f^{-0.443\pm0.007}$, which agrees with the slope of the total noise model, $f^{-0.450}$, within the 95% confidence interval. This result indicates that the measured data must have both Brownian noise and thermo-optic noise contributions to explain the fitted slope.

For further analysis, Fig. 7 shows three plots to illustrate the goodness of fit of our models to the measured data. The first panel, Fig. 7(a), shows a frequency spectrum of the measured data, Fig. 6 trace (i), minus the total noise model, Fig. 6 trace (iv). The second panel, Fig. 7(b), is a histogram of the data in 7(a). The result is a Gaussian distribution centered around 0, which indicates that the model captures any trends or offsets in the data. Figure 7(c) shows a contour plot of the normalized root mean square error (NRMSE) between the data and the model, when sweeping the unknown correction factors of the model. The sweep was done on the thermo-optic correction factors for higher order modes and the thick coating between 0 and 1.5, $\mathrm{C_{HOM\,TO}} \times \mathrm{C_{d\,TO}} \in (0, 1.5)$ and the Brownian noise thick coating correction factor also between 0 and 1.5, $\mathrm{C_{d\,BR}} \in (0, 1.5)$. The NRMSE was calculated at each of the sweep points, in each frequency bin of the data. NRMSE, given in Eq. (8), is a metric of standard deviation, which quantifies the error between modeled and measured values. y_i is the measured value for the ith data point, $\hat{y}_i$ is the modeled value for the ith data point, and N it the total number of data points:

$$\mathrm{NRMSE} = \frac{\sqrt{\frac{1}{N}\sum_{i=1}^{N}(y_i - \hat{y}_i)^2}}{y_{i,\max} - y_{i,\min}} \quad (8)$$

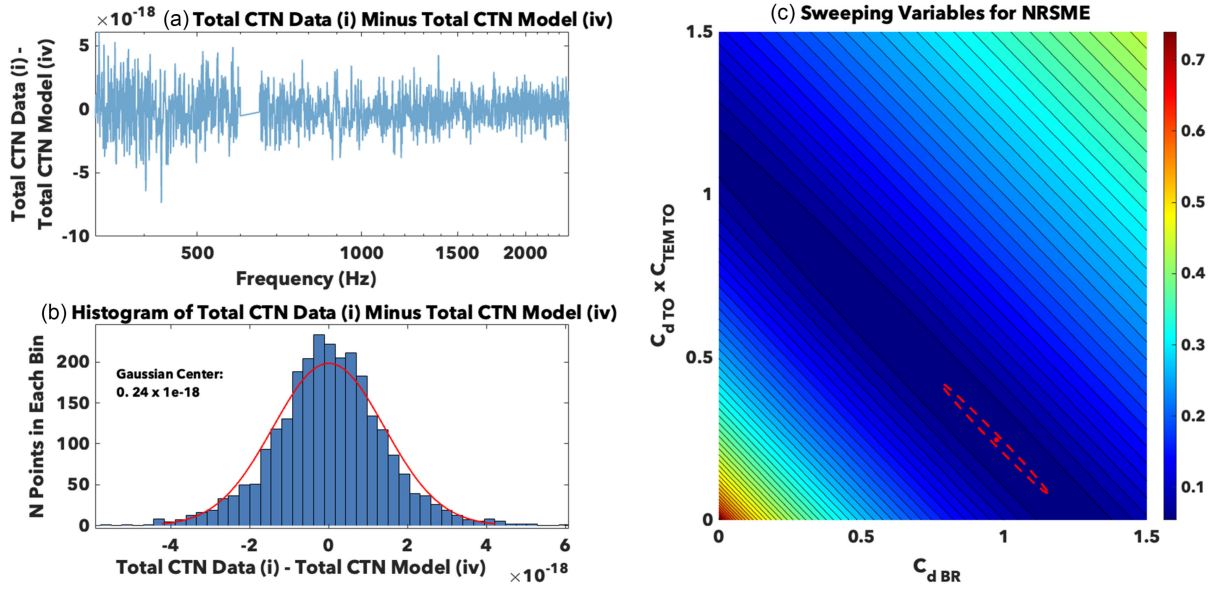


FIG. 7. Goodness of fit analysis of the data spectrum presented in Fig. 6. The peak at 600 Hz has been removed for this analysis. (a) Frequency spectrum of the thermal noise measurement, Fig. 6 trace (i), minus the total thermal noise model, Fig. 6 trace (iv). (b) Histogram of data from (a). The distribution is Gaussian and centered around 0, showing that the model is capturing all the trends and offsets in the data. (c) Contour plot of the normalized root mean square error (NRMSE) between the measured thermal noise and thermal noise model, while sweeping $\mathrm{C_{HOM\,TO}} \times \mathrm{C_{d\,TO}}$, the thermo-optic noise higher order mode and thick coating correction factors, and $\mathrm{C_{d\,BR}}$, the Brownian noise thick coating correction factor. The red data point reflects value of these correction factors used in the model, and the red line indicates the lowest 1% of NRMSE values to show that we have optimum fit with these values in the model with the measured data.

C. Implications for thermo-optic noise

A single red data point in Fig. 7(c) at $C_{HOM\,TO} \times C_{d\,TO} = 0.25$ and $C_{d\,BR} = 0.97$ is plotted to show the parameters used for the models in Figs. 6, 7(a), and 7(b) as reference. This data point is where the NRMSE is the lowest value. Furthermore, the lowest 1% of the contour plot is outlined in red, highlighting that we have the optimum fit to the data with these values. The contour plot indicates that the best fit of the model to the data requires some amount of thermo-optic noise to explain the slope and amplitude measured, and that Brownian noise cannot singularly explain the measured data, even when sweeping the slope and amplitude. Table I shows that the mechanical loss angle and frequency dependencies used in the model, which are $\phi_{nL} = 1.26 \times 10^{-4} \times f^{-0.069}$ for silica and $\phi_{nH} = 2.29 \times 10^{-4} \times f^{0.079}$ for tantala [29]. It should be noted, however, that there is still disagreement within current literature about the value of the mechanical loss angles for these materials at various frequencies [29,31–34], as well as the frequency dependencies themselves [29,33,34]. Therefore, this is also a source of uncertainty in our models for Brownian noise, and the inferred correction factors for Brownian noise and thermo-optic noise, $C_{HOM\,TO}$, $C_{d\,TO}$, and $C_{d\,BR}$. Future work involving a finite element analysis to accurately calculate these correction factors might allow us to use our data to predict the values of silica and tantala mechanical loss angles and frequency dependencies using a similar method of minimizing NRMSE.

D. Dependence on beam spot size

The same measurement as shown in Fig. 6 was repeated on sample 2 while varying the beam spot size on the sample mirror. The beam spot on the sample mirror was varied by moving the input coupler towards the sample mirror and output coupler away from the sample mirror by the same amount, such that the position of the cavity waist was shifted relative to the sample mirror, while maintaining the overall cavity length. Based on the models, Brownian noise is inversely linearly proportional to the beam size in amplitude spectral density. Thermo-optic noise is also inversely linearly proportional to beam size in amplitude spectral density, with further dependence on beam size in the lower frequencies that can effect the slope of the thermo-optic noise component. These effects couple into the total coating thermal noise (CTN), such that an increase in beam size will show a reduction in total CTN amplitude, as well as a small increase in slope.

The measured datasets were converted into linear form using the base 10 logarithmic function then fitted with a linear fitting function with a 95% confidence interval serving as error margins. The results from this data and the fitting function are shown in Table V, which presents the measurements for three beam sizes, $w_1 = 40$ μm, $w_2 = 44$ μm, and $w_3 = 48$ μm, as well as the relevant models for comparison. The amplitude values are reported in units of $\times 10^{-17} \frac{m}{\sqrt{Hz}}$ at 1 kHz. For w_1, the measured amplitude is 1.72 ± 0.08, and the modeled amplitude is 1.81. For w_2, the measured amplitude is 1.62 ± 0.08, and the modeled amplitude is 1.65. For w_3, the measured amplitude is 1.48 ± 0.07, and the modeled amplitude is 1.51. There is good consistency between modeled amplitudes and measured amplitudes, within the 95% confidence interval, and therefore we confirm that an increase in beam size reduces the magnitude of both Brownian and thermo-optic noise.

The measured slope for w_1 is -0.447 ± 0.007 and the modeled slope is -0.450. The measured slope for w_2 is -0.440 ± 0.007 and the modeled slope is -0.451. The measured slope for w_3 is -0.445 ± 0.007 and the modeled slope is -0.451. While the modeled and measured slopes mostly agree within the 95% confidence interval, it is not as clear that the data follows a trend of increasing slope. This is likely due to the data being dominated by Brownian noise and as such it is harder to be certain of the thermo-optic component changing slope in this frequency range. Further measurements of thermo-optic noise at lower frequencies are required to confirm that it indeed increases in slope with an increasing beam size, as predicted by the models. Furthermore, the correction factors shown in Sec. VI were used for all three beam sizes; however, it is likely that the thick coating correction for Brownian noise $C_{d\,BR}$ and thermo-optic noise $C_{d\,TO}$ change with beam size, as this correction factor is proportional to the ratio between beam

TABLE V. Beam spot size vs total coating thermal noise models and measurements made on sample 2, including linearly fitted amplitude and slope. All amplitude values are in amplitude spectral density units ($\times 10^{-17} \frac{m}{\sqrt{Hz}}$) and the slope is applied as the frequency dependence (f^{slope}) of the data.

Total CTN	$w_1 = 40$ μm	$w_2 = 44$ μm	$w_3 = 48$ μm
Fit to linearized data	$10^{-15.42\pm0.02} f^{-0.447\pm0.007}$	$10^{-15.47\pm0.02} f^{-0.440\pm0.007}$	$10^{-15.50\pm0.02} f^{-0.445\pm0.007}$
Measured amplitude at 1 kHz	1.72 ± 0.08	1.62 ± 0.08	1.48 ± 0.07
Modeled amplitude at 1 kHz	1.81	1.65	1.51
Measured slope	-0.447 ± 0.007	-0.440 ± 0.007	-0.445 ± 0.007
Modeled slope	-0.450	-0.451	-0.451

size and coating thickness. Finite element analysis is required to confirm this, but this source of uncertainty could explain the small deviations between the modeled and measured amplitude and slope of the coating thermal noise.

VIII. CONCLUSION

A novel coating with high coating Brownian thermal noise was designed for a future experiment. The first measurement to our knowledge of thermo-optic noise in a SiO_2:Ta_2O_5 coating was presented and experimentally verified.

The total coating thermal noise was measured to be $(1.81 \pm 0.08) \times 10^{-17} \times (\frac{1\,\mathrm{kHz}}{f})^{0.443\pm0.007}\ \frac{\mathrm{m}}{\sqrt{\mathrm{Hz}}}$, which is consistent with a modeled total coating thermal noise of $1.81 \times 10^{-17} \times (\frac{1\,\mathrm{kHz}}{f})^{0.450}\ \frac{\mathrm{m}}{\sqrt{\mathrm{Hz}}}$. Brownian noise contributes 77% to this total noise, with a modeled noise of $1.59 \times 10^{-17} \times (\frac{1\,\mathrm{kHz}}{f})^{0.47}\ \frac{\mathrm{m}}{\sqrt{\mathrm{Hz}}}$ and thermo-optic noise contributes 23% to this total noise with a modeled noise of $0.86 \times 10^{-17} \times (\frac{1\,\mathrm{kHz}}{f})^{0.38}\ \frac{\mathrm{m}}{\sqrt{\mathrm{Hz}}}$. With mechanical loss angles of $\phi_{\mathrm{nL}} = 1.26 \times 10^{-4} \times f^{-0.069}$ for silica and $\phi_{\mathrm{nH}} = 2.29 \times 10^{-4} \times f^{0.079}$ [29], we find the best fit using the correction factors $C_{\mathrm{HOM\,TO}} \times C_{\mathrm{d\,TO}} = 0.25$ and $C_{\mathrm{d\,BR}} = 0.97$. We also confirm that increasing the beam size, w, will decrease the magnitude of Brownian noise and thermo-optic noise.

ACKNOWLEDGMENTS

This research was supported by the Australian Research Council Centre of Excellence for Gravitational Wave Discovery (OzGrav, CE230100016), the Australian Research Council Centre of Excellence for Engineered Quantum Systems (EQUS, CE170100009). Kirk McKenzie is supported by SmartSat CRC's, funded by the Australian Government's CRC Program. The authors would also like to acknowledge the support of the LIGO Scientific Collaboration. LIGO was constructed by the California Institute of Technology and Massachusetts Institute of Technology with funding from the National Science Foundation, and operates under Cooperative Agreement No. PHY-1764464.

DATA AVAILABILITY

The data are not publicly available. The data are available from the authors upon reasonable request.

[1] A. Buikema *et al.*, Phys. Rev. D **102**, 062003 (2020).
[2] European Space Agency, LISA Factsheet (2024) (accessed: 2024-02-14).
[3] K. Abich *et al.*, Phys. Rev. Lett. **123**, 031101 (2019).
[4] NASA Earth Science, Decadal Survey: Most Complete Earth Science Study (2024) (accessed: 2024-02-14).
[5] A. D. Ludlow, X. Huang, M. Notcutt, T. Zanon-Willette, S. M. Foreman, M. M. Boyd, S. Blatt, and J. Ye, Opt. Lett. **32**, 641 (2007).
[6] A. D. Ludlow, M. M. Boyd, J. Ye, E. Peik, and P. O. Schmidt, Rev. Mod. Phys. **87**, 637 (2015).
[7] S. Herrmann, A. Senger, K. Möhle, M. Nagel, E. V. Kovalchuk, and A. Peters, Phys. Rev. D **80**, 105011 (2009).
[8] L. Barsotti, S. Gras, M. Evans, and P. Fritschel, Technical Note: The updated Advanced LIGO design curve, Technical Report No. T1800044-v5, Laser Interferometer Gravitational Wave Observatory, 2018 (accessed: 2024-02-14).
[9] S. Gras, H. Yu, W. Yam, D. Martynov, and M. Evans, Phys. Rev. D **95**, 022001 (2017).
[10] G. Vajente, L. Yang, A. Davenport, M. Fazio, A. Ananyeva, L. Zhang, G. Billingsley, K. Prasai, A. Markosyan, R. Bassiri, M. M. Fejer, M. Chicoine, F. Schiettekatte, and C. S. Menoni, Phys. Rev. Lett. **127**, 071101 (2021).
[11] K. Craig, J. Steinlechner, P. G. Murray, A. S. Bell, I. Birney, K. Haughian, J. Hough, I. MacLaren, S. Penn, S. Reid, R. Robie, S. Rowan, and I. W. Martin, Phys. Rev. Lett. **122**, 231102 (2019).
[12] A. Wade and K. McKenzie, Phys. Rev. A **106**, 023511 (2022).
[13] J. Steinlechner, Phil. Trans. R. Soc. A **376**, 20170282 (2018).
[14] M. Bondarescu, O. Kogan, and Y. Chen, Phys. Rev. D **78**, 082002 (2008).
[15] T. Chalermsongsak, E. D. Hall, G. D. Cole, D. Follman, F. Seifert, K. Arai, E. K. Gustafson, J. R. Smith, M. Aspelmeyer, and R. X. Adhikari, Metrologia **53**, 860 (2016).
[16] T. Hong, H. Yang, E. K. Gustafson, R. X. Adhikari, and Y. Chen, Phys. Rev. D **87**, 082001 (2013).
[17] W. Yam, S. Gras, and M. Evans, Phys. Rev. D **91**, 042002 (2015).
[18] S. C. Tait, J. Steinlechner, M. M. Kinley-Hanlon, P. G. Murray, J. Hough, G. McGhee, F. Pein, S. Rowan, R. Schnabel, C. Smith, L. Terkowski, and I. W. Martin, Phys. Rev. Lett. **125**, 011102 (2020).
[19] M. Evans, S. Ballmer, M. Fejer, P. Fritschel, G. Harry, and G. Ogin, Phys. Rev. D **78**, 102003 (2008).
[20] V. B. Braginsky, M. L. Gorodetsky, and S. P. Vyatchanin, Phys. Lett. A **271**, 303 (2000).
[21] Y. Levin, Phys. Lett. A **372**, 1941 (2008).
[22] M. J. Martin, Quantum metrology and many-body physics: Pushing the frontier of the optical lattice clock, PhD thesis, University of Colorado, 2013.
[23] V. B. Braginsky, M. L. Gorodetsky, and S. P. Vyatchanin, Phys. Lett. A **264**, 1 (1999).

[24] J. Talghader and J. S. Smith, Appl. Phys. Lett. **69**, 2608 (1996).
[25] N. Demos and S. Gras (private communication).
[26] G. Venugopalan, F. Salces-Cárcoba, K. Arai, and R. X. Adhikari, Opt. Express **32**, 11751 (2024).
[27] M. Notcutt, Personal email to the author regarding material specifications, Stable Laser Systems Supplier Communication (2023).
[28] G. M. Harry, H. Armandula, E. D'Ambrosio, P. Fritschel, M. E. Gustafson, D. R. M. Crooks, J. Hough, S. Rowan, P. Murray, M. Fejer, R. Route, and S. D. Penn, Phys. Rev. D **70**, 082003 (2004).
[29] M. Granata, A. Amato, L. Balzarini, M. Canepa, J. Degallaix, D. Forest, V. Dolique, L. Mereni, C. Michel, L. Pinard, B. Sassolas, J. Teillon, and G. Cagnoli, Classical Quantum Gravity **37**, 095004 (2020).
[30] D. Heinert, K. Craig, H. Grote, S. Hild, H. Lück, R. Nawrodt, D. A. Simakov, D. V. Vasilyev, S. P. Vyatchanin, and H. Wittel, Phys. Rev. D **90**, 042001 (2014).
[31] S. D. Penn, G. M. Harry, A. M. Gretarsson, S. E. Kittelberger, P. R. Saulson, J. J. Schiller, J. R. Smith, and L. Wallace, Classical Quantum Gravity **20**, 2917 (2003).
[32] M. Principe, I. M. Pinto, V. Pierro, R. DeSalvo, I. Taurasi, A. E. Villar, E. D. Black, K. G. Libbrecht, C. Michel, N. Morgado, and L. Pinard, Phys. Rev. D **91**, 022005 (2015).
[33] A. Amato, G. Cagnoli, M. Canepa, E. Coillet, J. Degallaix, V. Dolique, D. Forest, M. Granata, V. Martinez, C. Michel, L. Pinard, B. Sassolas, and J. Teillon, J. Phys. Conf. Ser. **957**, 012006 (2018).
[34] S. Gras and M. Evans, Phys. Rev. D **98**, 122001 (2018).

Correction: The previously published Fig. 6 contained an axis-label error and was replaced.